

# Space Maneuvering Target Integration Detection and Parameter Estimation for a Spaceborne Radar System With Target Doppler Aliasing

Muyang Zhan<sup>1</sup>, Graduate Student Member, IEEE, Penghui Huang<sup>2</sup>, Member, IEEE, Xingzhao Liu<sup>3</sup>, Member, IEEE, Guisheng Liao, Senior Member, IEEE, Zhijun Zhang, Zhicheng Wang, and Qingyu Hou

**Abstract**—Space maneuvering target detection and parameter estimation are the challenging problems in a spaceborne radar system. The complex motion of an observed target usually leads to the range migration (RM) and Doppler frequency migration, causing the difficulty in target detection. Furthermore, the relative high speed of space maneuvering target and limited pulse repetition frequency will result in Doppler ambiguity, further degrading the target detection performance. In this article, a novel and efficient coherent accumulation algorithm is proposed, which considers the velocity ambiguity and Doppler aliasing caused by the target radial velocity and acceleration, respectively. In the proposed method, the target radial velocity and acceleration are first separated by applying the time reversal transform technique. Then, the target radial velocity is estimated by using the Keystone transform. After compensating the velocity effects, the frequency reversal transform is proposed to remove the residual RM, and the acceleration estimation can be efficiently accomplished by the nonuniform fast Fourier transform. Compared with the conventional coherent integration methods, the proposed method can be suitable for the motion parameter estimation and coherent integration detection for a maneuvering target with velocity ambiguity and spectrum aliasing. Additionally, the proposed method is computationally efficient since only the complex multiplication and fast Fourier transform calculations are involved. Both simulation experiments and measured data results are provided to verify the effectiveness of the proposed algorithm.

**Index Terms**—Doppler aliasing, keystone transform (KT), motion parameter estimation, nonuniform fast Fourier transform (NUFFT), space maneuvering target detection, velocity ambiguity.

Manuscript received December 31, 2019; revised April 11, 2020 and May 26, 2020; accepted June 14, 2020. Date of publication June 19, 2020; date of current version July 2, 2020. This work was supported in part by the National Key R&D Program of China under Grant 2017YFB0502700, in part by the National Natural Science Foundation Program of China under Grant 61801289, and in part by the Natural Science Foundation of Shanghai under Grant 17ZR1428700. (Corresponding author: Penghui Huang.)

Muyang Zhan, Penghui Huang, and Xingzhao Liu are with the School of Electronic Information and Electrical Engineering, Shanghai Jiao Tong University, Shanghai 200240, China (e-mail: zhan\_sjtu@sjtu.edu.cn; huangpenghui@sjtu.edu.cn; xzliu@sjtu.edu.cn).

Guisheng Liao is with the National Laboratory of Radar Signal Processing, Xidian University, Xian 710071, China (e-mail: liaogs@xidian.edu.cn).

Zhijun Zhang is with the Shanghai Radio Equipment Research Institute, Shanghai 200090, China (e-mail: zjzweb@sohu.com).

Zhicheng Wang is with the School of Electronic Information and Electrical Engineering, Shanghai Jiao Tong University, Shanghai 200240, China, and also with the Shanghai Radio Equipment Research Institute, Shanghai 200090, China (e-mail: wangzhicheng@sjtu.edu.cn).

Qingyu Hou is with the 8511 Research Institute of China Aerospace Science and Industry Corporation, Nanjing 210007, China (e-mail: qyh1981@163.com).

Digital Object Identifier 10.1109/JSTARS.2020.3003809

This work is licensed under a Creative Commons Attribution 4.0 License. For more information, see <https://creativecommons.org/licenses/by/4.0/>

## I. INTRODUCTION

HIGH-SPEED maneuvering target detection has drawn increasing attention in recent years, especially in spaceborne early warning radar [1]–[5]. Long-time coherent integration is an effective technique to increase the target output signal-to-clutter and noise ratio (SCNR), which greatly improves the moving target detection performance, especially for the space weak targets, such as near-space hypersonic target, ballistic missile, and space debris. However, due to the complex motions of these types of maneuvering targets, range migration (RM) and Doppler frequency migration (DFM) will inevitably occur during the coherent processing interval, degrading the moving target coherent integration performance. Therefore, in order to achieve the effective target accumulation, the RM and DFM should be precisely compensated.

To address these issues, many effective solutions have been proposed in [6]–[36]. As for a moving target with uniform motion, some typical algorithms, such as the Keystone transform (KT) [6], [7], Radon Fourier transform (RFT) [8]–[9], axis rotation moving target detection (AR-MTD) [10], scaled inverse Fourier transform (SCIFT) [11], and frequency-domain Deramp-KT (FDDKT) [12] are widely used to accomplish the target coherent integration along the linear motion trajectory, which can exhibit the better integration detection performance compared with the noncoherent methods, such as Hough, Radon transform based methods [13]–[17]. In order to increase the target detection ability for a maneuvering target with accelerated motion, many alternative approaches have been proposed in the recent literatures, which can be mainly categorized into three types. The first type is the Radon-based methods, including the generalized RFT (GRFT) [18], Radon-fractional Fourier transform (RFRFT) [19], Radon-Lv's distribution [20], and joint time-frequency analysis methods [21]–[26]. These methods may suffer from heavy computational complexity as the multidimensional search is required to obtain target moving trajectory in the range compression domain. To alleviate the calculated burden, the second type of coherent integration methods based on the azimuth time domain or Doppler domain matched filtering processing is proposed, such as the 2-D matched filtering method [27], series reversion method [28], and KT matched filtering (KTMF) method [29], [30], which can effectively increase the calculation efficiency since the searched dimension is reduced.

However, these methods may not be suitable for the parameter estimation and focusing of a moving target with the low azimuth time–bandwidth product. To deal with this issue, the third type of methods based on modified KT is proposed; typical methods including the second-order KT (SOKT) [31]–[33], Doppler KT [34]–[35], and Deramp-Keystone processing [36], which can be suitable for the multiple target integration under the relatively low SNR case.

In a spaceborne early warning radar, in order to increase the range unambiguous observation scope, the pulse repetition frequency (PRF) may be limited to satisfy the large range observation area requirement. Then, for a high maneuverability space target, it is highly possible that both the velocity ambiguity and Doppler aliasing caused by radial acceleration exist and their effects may not be ignored in the integration time of seconds long, which makes the above-mentioned algorithms become more challengeable. As for the velocity ambiguity, the KT-based methods [29]–[33] require to search the velocity ambiguity number in order to eliminate the residual RM effects caused by the velocity ambiguity. Hough and Radon transform methods [13]–[17] still work for target with velocity ambiguity, whereas the poor efficiency caused by interpolation operation and low detection performance due to incoherent accumulation restricts its application. In addition, the Radon-based methods [18]–[20] have natural advantages in processing velocity ambiguity targets by expanding the searching area. However, the blind speed side-lobe (BSSL) occurs in this case, which will lead to the serious false alarm, especially for the low-resolution early warning radar system.

Nevertheless, when the velocity ambiguity and Doppler aliasing caused by target radial acceleration coexist, the target detection performance by using the above-mentioned methods may significantly degrade since the velocity ambiguity and Doppler aliasing will make the coupling relationship between range and azimuth more complex and stickier.

In this article, a novel search-free solution is proposed to realize the effective coherent accumulation for space maneuvering target, which considers velocity ambiguity and Doppler aliasing simultaneously. At first, conventional KT-based methods are introduced for velocity ambiguity and Doppler aliasing targets. Some characteristics of Doppler aliasing targets are also analyzed. Then, the proposed target detection and parameters estimation method is described in detail. In the proposed method, velocity and acceleration parts are separated by time reversal transform (TRT), and the KT is used for target detection and true velocity estimation. In the next, frequency reversal transform (FRT) is proposed to remove the residual RM, and nonuniform fast Fourier transform (NUFFT) is adopted to estimate true acceleration. In addition, the computational complexity and multicomponent signal analysis are discussed. Finally, the point target simulation, performance analysis, and real data processing results are provided to the validity of the proposed method. Compared with traditional target detection methods, the proposed method has the following merits.

1) The proposed method can obtain the better target detection performance than traditional methods for Doppler aliasing targets.

2) The proposed method is efficient since searching operation is avoided and only the complex multiplication and fast Fourier transform (FFT) calculations are involved.

The remainder of this article is organized as follows. Section II establishes the signal model of a space maneuvering target. The conventional algorithms are analyzed in Section III. Section IV introduces the proposed target detection and parameter estimation method in detail. In Section V, some performances are discussed. Section VI presents simulated and real data processing results and gives discussions to validate the proposed method. Finally, conclusion is drawn in Section VII.

## II. SIGNAL MODEL

Suppose that the radar transmits a linear frequency modulated signal, i.e.,

$$s(t_r) = \text{rect}(t_r/T_p) \exp\{j2\pi[f_c t_r + \gamma t_r^2/2]\} \quad (1)$$

where  $\text{rect}(\cdot)$  is the rectangle window function, i.e., it is equal to one for  $|t_r/T_p| \leq 1/2$ , and zeros for others.  $t_r$  is the range time (fast-time) variable,  $T_p$  is the pulse duration time,  $f_c$  is the carrier frequency, and  $\gamma$  is the chip rate of transmitted signal.

For high maneuvering target, the instantaneous slant range between the radar and target can be usually expressed as [37]

$$R(t_m) = R_0 + vt_m + \frac{1}{2}\alpha t_m^2 \quad (2)$$

where  $R_0$ ,  $v$ , and  $\alpha$  are the target initial slant range, radial velocity, and radial acceleration, respectively.  $t_m$  is the azimuth time (slow-time) variable, i.e.,  $t_m = m \cdot \text{PRT}$ , where PRT is the pulse repetition time (PRT) and  $m = [-M/2, -M/2 + 1, \dots, M/2]$  denotes the pulse number index, where  $M$  is set as an even integer for simplicity.

The received radar echoes after downconversion and pulse compression can be written as [38]

$$s(f_r, t_m) = \sigma \text{rect}\left(\frac{f_r}{B}\right) \text{rect}\left(\frac{t_m}{T_a}\right) \times \exp\left[-j\frac{4\pi(f_r + f_c)}{c}\left(R_0 + vt_m + \frac{1}{2}\alpha t_m^2\right)\right] \quad (3)$$

where  $\sigma$  is the signal complex amplitude in  $f_r - t_m$  domain,  $B$  is the signal bandwidth,  $T_a$  is the coherent accumulation time, and  $f_r$  is the range frequency variable.

After performing the inverse FFT (IFFT) on (3) along  $f_r$ , the echo signal in the 2-D time domain can be noted as

$$s(t_r, t_m) = A \text{rect}\left(\frac{t_r}{T_p}\right) \text{rect}\left(\frac{t_m}{T_a}\right) \times \sin c\left[B\left(t_r - 2\left(R_0 + vt_m + \frac{1}{2}\alpha t_m^2\right)/c\right)\right] \times \exp\left[-j\frac{4\pi}{\lambda}\left(R_0 + vt_m + \frac{1}{2}\alpha t_m^2\right)\right] \quad (4)$$

where  $A$  is the amplitude in the 2-D time domain,  $\lambda$  is the wavelength, and  $\text{sinc}(x) = \sin(\pi x)/\pi x$  represents the sinc function. It can be seen from (4) that the target radial velocity will cause the linear range walk and the radial acceleration will introduce the range curvature, significantly degrading the target detection performance. Additionally, the Doppler phase broadening caused by the acceleration component will be present, which should be compensated with a higher precision since the broadened Doppler is compared with the signal wavelength.

Usually, for a spaceborne early warning radar, the PRT may be large enough to realize a large observation range. Then, for a high-speed moving target, it is highly possible that the Doppler frequency induced by the target radial velocity exceeds PRF, i.e., the velocity ambiguity occurs. Then, the Doppler frequency induced by the target radial velocity can be rewritten as

$$f_{d,v} = \frac{2v}{\lambda} = \frac{2v_b}{\lambda} + M_v \text{PRF} \quad (5)$$

where  $v = v_b + M_v \cdot v_{\text{amb}}$ ,  $v_b$  is the unambiguous velocity satisfying  $|v_b| \leq v_{\text{amb}}/2$ ,  $M_v$  is the velocity ambiguity number,  $v_{\text{amb}} = \lambda \text{PRF}/2$  is the blind velocity of radar, and PRF is pulse repetition frequency.

There are three main methods for speed compensation in this case. The first class of methods is the KT-based methods [29]–[33], which requires searching  $M_v$  in order to eliminate the residual RM effects caused by the velocity ambiguity term. The second kind of methods is the Hough and Radon transform methods [13]–[17], which can be used by estimating slope with target moving trajectory while suffering from the low efficiency and poor incoherent detection performance. The third class of methods is the Radon-based methods [18]–[20], which can handle the velocity ambiguity by expanding the searching area. However, it will further increase the computation costs and the BSSL occurs in this case, which will lead to serious false alarm.

In addition, when the acceleration of the target is also ambiguous, the coupling characteristics will become very complex and the coherent integration performance of the traditional methods may significantly degrade. In this case, Doppler frequency can be expressed as

$$f_d = f_{d,v} + f_{d,\alpha} \quad (6)$$

where  $f_{d,\alpha}$  represent the Doppler frequency induced by the radial acceleration. Under the circumstances of the target high speed and radar low PRF, it is highly possible that Doppler ambiguity and Doppler aliasing would simultaneously occur. The velocity ambiguity number and Doppler aliasing number can be calculated as

$$\begin{cases} M_v = \left\lceil \frac{f_{d,v} - \text{PRF}/2}{\text{PRF}} \right\rceil \\ M_\alpha = \left\lceil \frac{f_{d,\alpha} - \text{PRF}/2}{\text{PRF}} \right\rceil \end{cases} \quad (7)$$

where  $M_\alpha$  is the Doppler aliasing number, and  $\lceil \cdot \rceil$  represents round up operation.

As previously mentioned, the velocity ambiguity can be solved by searching ambiguity numbers [29]–[30], while Doppler aliasing caused by the radial acceleration make the coupling relationship between range and azimuth more complicated

and stickier. In the next section, the mathematical derivation and some characteristics for velocity ambiguity and Doppler aliasing target are presented.

### III. CONVENTIONAL KT-BASED ALGORITHM ANALYSIS

In this section, the coherent integration performance of the conventional detection methods for a high-speed and maneuvering target with velocity ambiguity and Doppler aliasing are briefly analyzed.

#### A. Coherent Integration for a Velocity Ambiguous Target

In the following, we first consider the coherent integration of a uniformly moving target with the velocity ambiguity, whose expression in the range-frequency domain is given by

$$\begin{aligned} S(f_r, t_m) &= \sigma \text{rect} \left( \frac{f_r}{B} \right) \text{rect} \left( \frac{t_m}{T_a} \right) \exp \left[ -j \frac{4\pi (f_r + f_c)}{c} R_0 \right] \\ &\times \exp \left[ -j \frac{4\pi (f_r + f_c)}{c} v_b t_m \right] \\ &\times \exp \left[ -j 2\pi \frac{f_r}{f_c} M_v \text{PRF} t_m \right] \\ &\times \exp \left[ -j 2\pi M_v \text{PRF} t_m \right]. \end{aligned} \quad (8)$$

Considering that the last term of (8) is an integral multiple of  $2\pi$ , (8) can be further simplified as

$$\begin{aligned} S(f_r, t_m) &= \sigma \text{rect} \left( \frac{f_r}{B} \right) \text{rect} \left( \frac{t_m}{T_a} \right) \exp \left[ -j \frac{4\pi (f_r + f_c)}{c} R_0 \right] \\ &\times \exp \left[ -j \frac{4\pi (f_r + f_c)}{c} v_b t_m \right] \\ &\times \exp \left[ -j 2\pi \frac{f_r}{f_c} M_v \text{PRF} t_m \right]. \end{aligned} \quad (9)$$

In order to solve Doppler ambiguity induced by the target radial velocity, a typical solution in [29] and [30] is to perform the KT first, then compensate the phase term caused by velocity ambiguous terms. After performing the KT to eliminate the RM caused by target radial velocity, one has

$$\begin{aligned} S_{\text{KT}}(f_r, t_a) &= \sigma \text{rect} \left( \frac{f_r}{B} \right) \text{rect} \left( \frac{f_c}{f_r + f_c} \frac{t_a}{T_a} \right) \\ &\times \exp \left[ -j \frac{4\pi (f_r + f_c)}{c} R_0 \right] \exp \left[ -j \frac{4\pi}{\lambda} v_b t_a \right] \\ &\times \exp \left[ -j 2\pi \frac{f_r}{f_c} M_v \text{PRF} t_a \right] \\ &\times \exp \left[ j 2\pi \frac{f_r^2}{f_c^2} M_v \text{PRF} t_a \right] \end{aligned} \quad (10)$$

where  $t_a$  is new azimuth time variable after KT with  $(f_r + f_c)t_m = f_c t_a$ , and the derivation of (10) uses the approximation of  $f_c/(f_r + f_c) \approx 1 - f_r/f_c$ . It can be clearly seen from (10) that the residual range walk in virtue of ambiguous velocity component is present, which can be further compensated via the

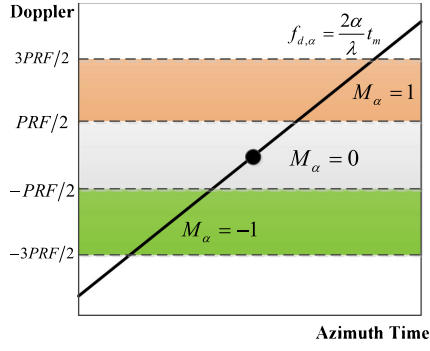


Fig. 1. Time-varied Doppler frequency induced by the acceleration.

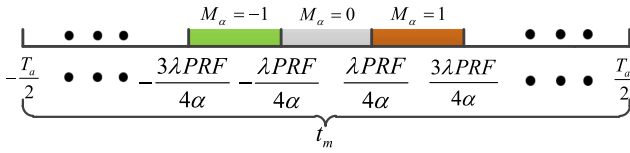


Fig. 2. Azimuth time division according to the different Doppler ambiguity numbers.

phase compensation function given by

$$H_{\text{com}} = \exp \left[ j2\pi \frac{f_r}{f_c} M_v \text{PRF} t_a \right] \exp \left[ -j2\pi \frac{f_r^2}{f_c^2} M_v \text{PRF} t_a \right]. \quad (11)$$

### B. Coherent Integration for a Doppler Aliased Target

In this section, we consider a highly maneuvering target that is only with a radial acceleration for simplicity, i.e.,

$$s(f_r, t_m) = \sigma \text{rect} \left( \frac{f_r}{B} \right) \text{rect} \left( \frac{t_m}{T_a} \right) \times \exp \left[ -j \frac{4\pi (f_r + f_c)}{c} \left( R_0 + \frac{1}{2} \alpha t_m^2 \right) \right]. \quad (12)$$

The Doppler frequency caused by the acceleration component can be noted as  $f_{d,\alpha} = 2\alpha t_m / \lambda$ . Different from Doppler frequency caused by the velocity, it should be pointed out that  $f_{d,\alpha}$  will cause the time-varied ambiguity numbers, as shown in Fig. 1.

From Fig. 1, it is observed that the Doppler aliasing number is time varying and the slow-time sequence can be divided into multiple intervals according to the different Doppler ambiguity numbers, which can be expressed as

$$t_{m,M_\alpha} = t_{m,-M_{\alpha,\max}} \cup \dots \cup t_{m,0} \cup \dots \cup t_{m,M_{\alpha,\max}} \quad (13)$$

where  $M_{\alpha,\max}$  is the maximum Doppler aliasing number,  $t_{m,-M_{\alpha,\max}} \in [-\frac{T_a}{2}, -\frac{\lambda \text{PRF}}{4\alpha} (M_{\alpha,\max} - 1)]$ ,  $t_{m,0} \in [-\frac{\lambda \text{PRF}}{4\alpha}, \frac{\lambda \text{PRF}}{4\alpha}]$ , and  $t_{m,M_{\alpha,\max}} \in [\frac{\lambda \text{PRF}}{4\alpha} (M_{\alpha,\max} - 1), \frac{T_a}{2}]$ . Fig. 2 shows the slow-time division according to the different Doppler aliasing numbers.

For convenience, take the Doppler aliasing times of integer multiples as an example. Define the total aliasing number

as  $M_s = 2M_{\alpha,\max} + 1$ . Then, the echo signal in the case of  $|f_{d,\alpha}| > \text{PRF}/2$  can be represented as a sum of multiple signal components with different aliasing numbers, that is

$$S(f_r, t_m) = \sum_{M_\alpha=-M_{\alpha,\max}}^{M_{\alpha,\max}} \sigma \text{rect} \left( \frac{f_r}{B} \right) \text{rect} \left( \frac{t_{m,M_\alpha}}{T_a/M_s} \right) \times \exp \left[ -j \frac{4\pi (f_r + f_c)}{c} \left( R_0 + \frac{1}{2} \alpha t_{m,M_\alpha}^2 \right) \right] \quad (14)$$

According to the relation between a signal with Doppler aliasing times  $M_\alpha$  and an unambiguous signal, (14) can be further rewritten as follows:

$$S(f_r, t_m) = \sum_{M_\alpha=-M_{\alpha,\max}}^{M_{\alpha,\max}} \sigma \text{rect} \left( \frac{f_r}{B} \right) \text{rect} \left( \frac{t_{m,M_\alpha}}{T_a/M_s} \right) \times \exp \left[ -j \frac{4\pi (f_r + f_c)}{c} \left( R_0 + \frac{1}{2} \alpha t_{m,0}^2 \right) \right] \times \exp \left[ -j2\pi \frac{f_r}{f_c} M_\alpha \text{PRF} t_{m,0} \right] \times \exp \left[ -j \frac{\pi (f_r + f_c)}{f_c} M_\alpha^2 \text{PRF} \frac{T_a}{M_s} \right]. \quad (15)$$

The detailed derivation of (15) is given in Appendix I. For the signal in (12), the range curvature is usually compensated by using the SOKT. Then, the target signal in (15) after the SOKT can be rewritten as

$$S(f_r, \tau_m) = \sum_{M_\alpha=-M_{\alpha,\max}}^{M_{\alpha,\max}} \text{rect} \left( \frac{f_r}{B} \right) \text{rect} \left( \frac{\tau_{m,M_\alpha}}{T_a} \right) \times \exp \left[ -j \frac{4\pi (f_r + f_c)}{c} R_0 \right] \exp \left[ -j \frac{2\pi}{\lambda} \alpha \tau_{m,M_\alpha}^2 \right] \times \exp \left[ -j2\pi \frac{f_r}{f_c} M_\alpha \text{PRF} \tau_{m,0} \right] \times \exp \left[ j\pi \frac{f_r^2}{f_c^2} M_\alpha \text{PRF} \tau_{m,0} \right] \times \exp \left[ -j \frac{\pi (f_r + f_c)}{f_c} M_\alpha^2 \text{PRF} \frac{T_a}{M_s} \right] \quad (16)$$

where  $\tau_m$  is the new azimuth time variable after KT with  $(f_r + f_c)t_m^2 = f_c \tau_m^2$  and  $\tau_{m,M_\alpha}$  has a similar definition in (13) as  $t_{m,M_\alpha}$ . The derivation of (16) uses the approximation of  $\sqrt{f_c/(f_r + f_c)} \approx 1 - f_r/(2f_c)$ . It is obvious that the range curve is eliminated after SOKT. However, the residual linear range walk term  $\exp[-j2\pi \frac{f_r}{f_c} M_\alpha \text{PRF} \tau_{m,0}]$  induced by the Doppler aliasing number is still present, and this range walk is piecewise along the slow-time axis since the Doppler aliasing number in different slow-time sequences is different. The penultimate term of (16) can be neglected due to the fact that  $f_r^2 \ll f_c^2$ . The last term of (16) leads to the range profile hopping with different Doppler aliasing numbers corresponding to the segmented slow-time sequences in (13). Therefore, when the Doppler aliasing caused by target acceleration is present, the SOKT may be invalid to correct the RM.

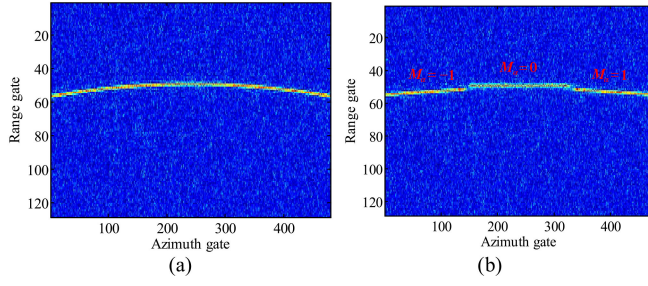


Fig. 3. Results before and after SOKT. (a) Range compression result. (b) Range curvature compensation by SOKT.

TABLE I  
RADAR SYSTEM PARAMETERS

Parameters	Value
Carrier frequency	1.3GHz
Range bandwidth	40MHz
Range sampling frequency	60MHz
Pulse repetition frequency	400Hz
Pulse duration time	0.5 $\mu$ s
Dwell time	1.2s

In order to better illustrate this phenomenon, a moving target simulation result is given in Fig. 3. The simulation radar parameters are listed in Table I, the range and azimuth sample numbers are 128 and 480, respectively, and the motion parameters of this maneuvering target is set as  $[R_0, v, \alpha] = [100 \text{ km}, 0 \text{ ms}, 100 \text{ m/s}^2]$ . The total Doppler aliasing number caused by acceleration can be calculated as 3.

From Fig. 3, it is clearly observed that the range walk of the unambiguous part is eliminated. However, the troubled issue is that the piecewise range walk and range profile hopping appear in the ambiguous parts after the SOKT because of the different Doppler aliasing numbers corresponding to different trajectory slopes, as forecast by (16).

### C. Coherent Integration for a Moving Target With Both the Velocity Ambiguous and Doppler Aliasing

For a high-speed and maneuvering target, when both the velocity ambiguity and Doppler aliasing exist, the target signal in the range-frequency domain can be expressed as

$$\begin{aligned}
 s(f_r, t_m) = & \sum_{M_\alpha = -M_{\alpha, \max}}^{M_{\alpha, \max}} \sigma \text{rect}\left(\frac{f_r}{B}\right) \text{rect}\left(\frac{t_m, M_\alpha}{T_a/M_s}\right) \\
 & \times \exp\left[-j\frac{4\pi}{c}(f_r + f_c)\left(R_0 + v_b t_m + \frac{1}{2}\alpha t_{m,0}^2\right)\right] \\
 & \times \exp\left[-j2\pi\frac{f_r}{f_c}M_v \text{PRF}t_m\right] \\
 & \times \exp\left[-j2\pi\frac{f_r}{f_c}M_\alpha \text{PRF}t_{m,0}\right] \\
 & \times \exp\left[-j\frac{\pi}{f_c}(f_r + f_c)M_\alpha^2 \text{PRF}\frac{T_a}{M_s}\right]. \quad (17)
 \end{aligned}$$

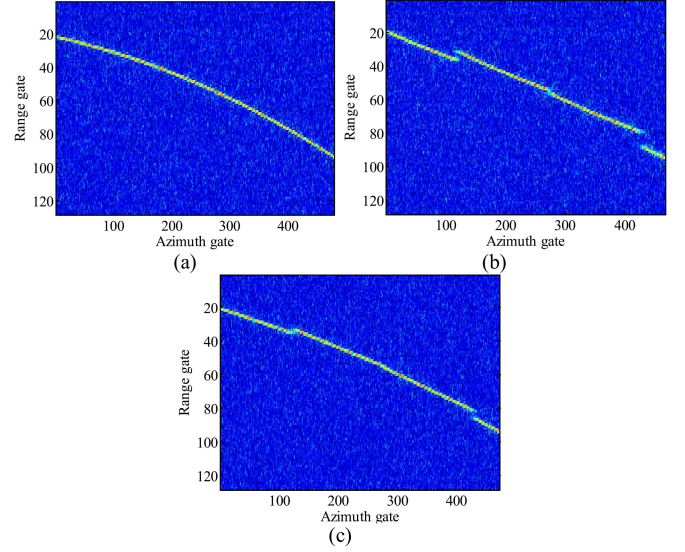


Fig. 4. Target motion trajectories before and after SOKT. (a) Target motion trajectory after range compression. (b) Range walk compensation by KT. (c) Range curvature compensation by SOKT.

It can be observed from (17) that the velocity ambiguity generates an extra range walk term over the whole dwell time, whereas the Doppler aliasing induced by acceleration exhibits the migration-segmented feature, making the range and azimuth coupling relationship more complex.

The following example shows the processing results for a moving target with velocity ambiguity and spectrum aliasing. The radial velocity and acceleration of moving target are set as 150 m/s and 120 m/s<sup>2</sup>, respectively, other parameters are the same as those used in Fig. 3. According to the radar and moving target parameters, the number of the velocity ambiguity is calculated as 3 and the total number of the Doppler aliasing is 3. The target motion trajectory is shown in Fig. 4(a), from which it is observed that the severe range walk and range curvature appear. Fig. 4(b) and (c) shows the range walk compensation result and the range curvature elimination result by using the KT and SOKT, respectively. Obviously, the target trajectory is split into multiple segments, indicating that the well-known KT- or SOKT-based techniques may be invalid in this case because these methods may not effectively resolve the complex coupling effects introduced by velocity ambiguity and spectrum aliasing.

## IV. PROPOSED METHOD

In this section, a new coherent integration method is proposed to realize the motion parameters estimation and focusing for a moving target with velocity ambiguity and Doppler aliasing. First, the target radial velocity is separated from the target motion slant range by using the TRT, and then the target velocity estimation is achieved by the traditional KT. In the next, the range curve correction and acceleration estimation can be implemented by the FRT and NUFFT.

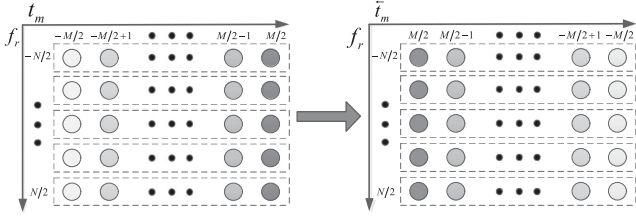


Fig. 5. Schematic diagram of the TR operation.

### A. Radial Velocity Removal and Estimation

The diagram of TR operation is shown in Fig. 5, which can be seen that TR operation [39] reorder the azimuth echo data.

The TR of (3) can be expressed as

$$s\left(f_r, \overleftarrow{t}_m\right) = \sigma \text{rect}\left(\frac{f_r}{B}\right) \text{rect}\left(\frac{-t_m}{T_a}\right) \times \exp\left[-j\frac{4\pi(f_r + f_c)}{c}\left(R_0 - vt_m + \frac{1}{2}\alpha t_m^2\right)\right]. \quad (18)$$

The TRT is defined as [39]

$$\begin{aligned} s_{\text{TRT}}(f_r, t_m) &= s(f_r, t_m) \left[s\left(f_r, \overleftarrow{t}_m\right)\right]^* \\ &= \sigma^2 \text{rect}\left(\frac{f_r}{B}\right) \text{rect}\left(\frac{t_m}{T_a}\right) \\ &\quad \times \exp\left[-j\frac{8\pi(f_r + f_c)}{c}vt_m\right]. \end{aligned} \quad (19)$$

It can be seen that quadratic range curvature is eliminated, while the range walk is double after the TRT. For velocity ambiguous target, we have

$$\begin{aligned} s_{\text{TRT}}(f_r, t_m) &= \sigma^2 \text{rect}\left(\frac{f_r}{B}\right) \text{rect}\left(\frac{t_m}{T_a}\right) \\ &\quad \times \exp\left[-j\frac{4\pi(f_r + f_c)}{c}2v_b t_m\right] \\ &\quad \times \exp\left[-j\frac{4\pi f_r}{f_c}M_v \text{PRF} t_m\right]. \end{aligned} \quad (20)$$

After performing the traditional KT to eliminate the RM caused by radial velocity, one has

$$\begin{aligned} s_{\text{TRT-KT}}(f_r, t_a) &= \sigma^2 \text{rect}\left(\frac{f_r}{B}\right) \text{rect}\left(\frac{f_c}{f_r + f_c}\frac{t_a}{T_a}\right) \exp\left[-j\frac{4\pi}{\lambda}2v_b t_a\right] \\ &\quad \times \exp\left[-j4\pi\frac{f_r}{f_c}M_v \text{PRF} t_a\right] \exp\left[j4\pi\frac{f_r^2}{f_c^2}M_v \text{PRF} t_a\right]. \end{aligned} \quad (21)$$

It can be seen from (21) that the residual range walk caused by the ambiguous velocity can be further compensated as

$$H_{\text{com},1} = \exp\left[j4\pi\frac{f_r}{f_c}M_v \text{PRF} t_a\right] \exp\left[-j4\pi\frac{f_r^2}{f_c^2}M_v \text{PRF} t_a\right]. \quad (22)$$

Obviously, when the ambiguity number is properly matched, the RM in (21) can be well compensated, with a moving target represented as a peak in the  $t_r - f_a$  domain, i.e.,

$$\begin{aligned} S_{\text{TRT-KT}}(t_r, f_a) &= \text{FFT}_{t_m}[\text{IFFT}_{f_r}[S_{\text{TRT-KT}}(f_r, t_m) \cdot H_{\text{com},1}]] \\ &= A_1 \sin c(Bt_r) \sin c\left[T_a\left(f_a + \frac{4v_b}{\lambda}\right)\right] \end{aligned} \quad (23)$$

where  $\text{FFT}_{t_m}$  and  $\text{IFFT}_{f_r}$  denote performing FFT along  $t_m$  and IFFT along  $f_r$ , respectively, and  $A_1$  is the complex amplitude in the  $t_r - f_a$  domain. Finally, the target radial velocity can be obtained by

$$\hat{v} = \left(\hat{M}_v \cdot v_{\text{amb}} + \hat{v}_b\right) / 2 \quad (24)$$

where  $\hat{v}_b = -\frac{\lambda}{4}f_a$  and  $\hat{M}_v$  is the estimated velocity ambiguity number.

### B. Doppler Chirp Parameter Estimation via FRT and NUFFT

From Section III, one can clearly see that the conventional KT-based method may be invalid for the Doppler parameter estimation for a maneuvering target with Doppler aliasing. To address this issue, a novel method based on FRT and NUFFT is proposed in this section.

According to (24), the target velocity component can be compensated in the range-frequency domain via the following compensation function:

$$H_{\text{com},2} = \exp\left[-j\frac{4\pi(f_r + f_c)}{c}\hat{v}t_m\right]. \quad (25)$$

After multiplying (3) by (25), one has

$$\begin{aligned} s(f_r, t_m) &= \sigma \text{rect}\left(\frac{f_r}{B}\right) \text{rect}\left(\frac{t_m}{T_a}\right) \\ &\quad \times \exp\left[-j\frac{4\pi(f_r + f_c)}{c}\left(R_0 + \frac{1}{2}\alpha t_m^2\right)\right]. \end{aligned} \quad (26)$$

Similar to the TR operation, the frequency reverse (FR) and FRT are, respectively, defined as follows:

$$\begin{aligned} s\left(\overleftarrow{f}_r, t_m\right) &= \sigma \text{rect}\left(\frac{-f_r}{B}\right) \text{rect}\left(\frac{t_m}{T_a}\right) \\ &\quad \times \exp\left[-j\frac{4\pi(-f_r + f_c)}{c}\left(R_0 + \frac{1}{2}\alpha t_m^2\right)\right] \end{aligned} \quad (27)$$

$$\begin{aligned} s_{\text{FRT}}(f_r, t_m) &= s(f_r, t_m) s\left(\overleftarrow{f}_r, t_m\right) \\ &= \sigma^2 \text{rect}\left(\frac{f_r}{B}\right) \text{rect}\left(\frac{t_m}{T_a}\right) \\ &\quad \times \exp\left[-j\frac{4\pi}{\lambda}(2R_0 + \alpha t_m^2)\right]. \end{aligned} \quad (28)$$

Schematic diagram of the FR operation is shown in Fig. 6.

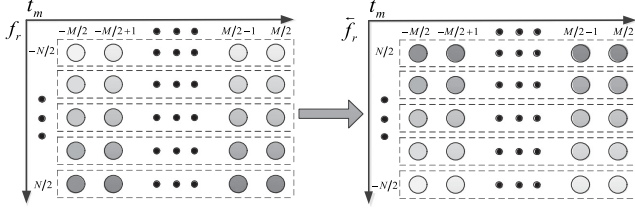


Fig. 6. Schematic diagram of FR operation.

It can be seen that the RM is removed by using the FRT. Performing IFFT to (28) along the range direction, one can obtain

$$s_{\text{FRT}}(t_r, t_m) = A_2 \sin c(Bt_r) \exp \left[ -j \frac{4\pi}{\lambda} (2R_0 + \alpha t_m^2) \right] \quad (29)$$

where  $A_2$  is the complex amplitude. It should be pointed out that the results of (28) and (29) is still valid for a Doppler aliasing target since the phase terms induced by ambiguous terms are also symmetric along the range frequency. Similarly to the ambiguous velocity, acceleration can be described as

$$\alpha = M_{\alpha, \max} \alpha_{\text{amb}} + \alpha_b \quad (30)$$

where  $\alpha_{\text{amb}} = \lambda \text{PRF} / (2T_a)$  and  $\alpha_b$  is the unambiguous acceleration which satisfies  $|\alpha_b| \leq \alpha_{\text{amb}}/2$ .

If the nonuniform discrete Fourier transform (NUDFT) is directly performed on (29) with respect to  $t_m^2$ ,  $\alpha$  cannot be effectively estimated due to the phase ambiguity. Therefore, the ambiguity acceleration component in (29) should be compensated in advance, which can be compensated as follows:

$$H_{\text{com},3} = \exp \left[ -j2\pi M_{\alpha} \text{PRF} t_m^2 / T_a \right]. \quad (31)$$

When the searching Doppler aliasing number matches the actual value, the residual Doppler phase term is expressed as

$$s_{\text{FRT}}(t_r, t_m) = A_2 \text{sinc}(Bt_r) \exp \left[ -j \frac{4\pi}{\lambda} (2R_0 + \alpha_b t_m^2) \right]. \quad (32)$$

After performing the NUDFT with respect to the nonlinear time variable  $t_m^2$ , one has

$$\begin{aligned} s_{\text{FRT-NUDFT}}(t_r, t_m) &= A_2 \sin c(Bt_r) \\ &\times \int \exp \left[ -j \frac{4\pi}{\lambda} (2R_0 + \alpha_b t_m^2) \right] \\ &\times \exp(-j2\pi f_{t_m}^2 t_m^2) dt_m^2 \\ &= A_3 \sin c(Bt_r) \sin c \left[ T_a \left( f_{t_m}^2 + \frac{2}{\lambda} \alpha_b \right) \right] \end{aligned} \quad (33)$$

where  $A_3$  is the complex amplitude after performing the NUDFT. Finally, the target radial acceleration can be estimated as

$$\hat{\alpha} = \left( \hat{\alpha}_b + \hat{M}_{\alpha} \alpha_{\text{amb}} \right) / 2 \quad (34)$$

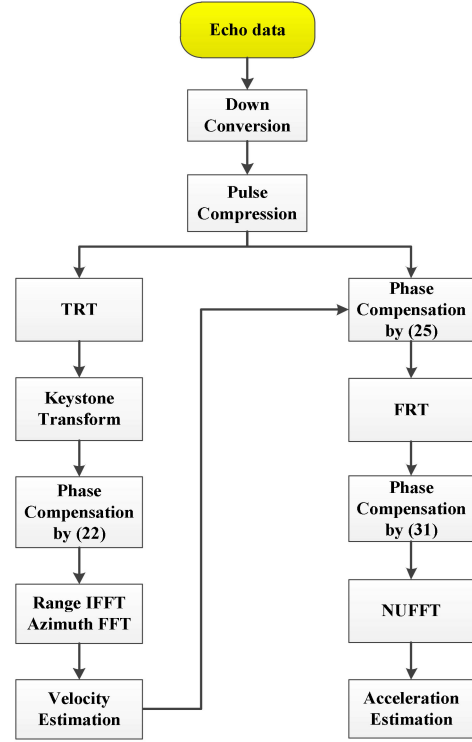


Fig. 7. Flowchart of the proposed method.

where  $\hat{\alpha}_b = -\frac{\lambda}{2} f_{t_m}^2$ , and  $\hat{M}_{\alpha}$  is the estimated Doppler aliasing number.

The essence of the NUDFT in (33) is the interpolation operation, which is time consuming, especially during a relatively long observation time. Fortunately, the time-consumed NUDFT in (33) can be accelerated by using the NUFFT [40], [41], with the low computation amount of  $O(N \log_2 N)$ . The corresponding description and implementation of NUFFT is given in Appendix II.

The flowchart of the proposed target detection and parameter estimation algorithm is shown in Fig. 7.

## V. COMPUTATION COMPLEXITY ANALYSIS AND MULTICOMPONENT SIGNAL ANALYSIS

In this section, the computational complexity of the proposed method and the other typical methods are analyzed first. Then, the multicomponent signal analysis is provided.

### A. Computational Complexity Analysis

Denote the number of range cells and azimuth cells as  $N_r$  and  $N_a$ , respectively, and ignore the computational burden caused by the addition operation. The TRT, FRT, and phase compensation operations have the computation cost with  $O(N_r N_a)$ . The computational complexity of the KT is  $O(4N_r N_a \log_2 N_a) + O(4N_r N_a)$  by adopting the scaling transform [42]. The NUFFT operation only involves the computation cost with  $O(N_a \log_2 N_a)$  instead of NUDFT with  $O(N_a^2)$ . As for the 2-D FFT, its computational complexity is  $O(N_r N_a \log_2 N_r + N_r N_a \log_2 N_a)$ . Therefore, the total computational complexity of the proposed method is about

TABLE II  
COMPUTATIONAL COMPLEXITY OF DIFFERENT METHODS

Methods	The computational complexity
GRFT method	$O(M_r^2 N_r N_a)$
RFRFT method	$O(M_r^2 M_p N_r N_a \log_2 N_a)$
KTMF method	$O[(K_1 + 4)N_r N_a + (M_r + K_1 + 4)N_r N_a \log_2 N_a]$
Proposed method	$O[(K_1 + 1)N_r N_a \log_2 N_r + (K_1 + K_2 + 7)N_r N_a + 4N_r N_a \log_2 N_a + (K_1 + K_2)N_a \log_2 N_a]$

$O[(K_1 + 1)N_r N_a \log_2 N_r + (K_1 + K_2 + 7)N_r N_a + 4N_r N_a \log_2 N_a + (K_1 + K_2)N_a \log_2 N_a]$ , where  $K_1$  and  $K_2$  are the searching numbers of ambiguity number of radial velocity and acceleration, respectively, which are usually very small since they are the integers distributed in a certain region. Assume that the searing times of the target radial velocity and acceleration are the same, denoted by  $M_t$ . As for the GRFT method, the computational complexity is about  $O(M_t^2 N_r N_a)$  due to the 2-D violent search [18]. The computation cost of the RFRFT method [19] is  $O(M_t^2 M_p N_r N_a \log_2 N_a)$  since the FrFT is used to focus the target on the basis of searching the target trajectory, where  $M_p$  is the searching order number in FrFT. The computational complexity of the KTMF method [29] involves a 1-D search for target's acceleration estimation, which is about  $O[(K + 4)N_r N_a + (M + K + 4)N_r N_a \log_2 N_a]$ . The detailed computational costs of the abovementioned methods are summarized in Table II.

### B. Multicomponent Signal Analysis

For multiple targets, due to the bilinearity of the TRT and FRT, the cross terms appear and may influence the detection and parameters estimation of the autoterms. In the following derivation, the influences of cross terms are analyzed. Consider a noise-free compressed signal for multitargets in range-frequency and azimuth-time domain as follows:

$$s(f_r, t_m) = \sum_{i=1}^I \sigma_i \exp \left[ -j \frac{4\pi(f_r + f_c)}{c} \left( R_i + v_i t_m + \frac{1}{2} \alpha_i t_m^2 \right) \right] \quad (35)$$

where  $I$  is the moving target number, and  $\sigma_i$ ,  $R_i$ ,  $v_i$ , and  $\alpha_i$  are the signal amplitude, the initial distance, the radial velocity, and acceleration of the  $i$ th target, respectively.

After performing the TRT, echo signal can be expressed as follows:

$$s_{\text{TRT}}(f_r, t_m) = s_{\text{TRT-auto}}(f_r, t_m) + \sum_{l=1}^{I-1} \sum_{q=l+1}^I s_{\text{TRT-}l,q\text{-cross}}(f_r, t_m) \quad (36a)$$

where

$$s_{\text{TRT-auto}}(f_r, t_m) = \sum_{i=1}^I \sigma_i^2 \exp \left[ -j \frac{8\pi(f_r + f_c)}{c} v_i t_m \right] \quad (36b)$$

denotes the autoterms and  $s_{\text{TRT-}l,q\text{-cross}}(f_r, t_m)$  is the cross term generated by the  $l$ th target and the  $q$ th target, whose expression is given in Appendix III. The autoterms only contain the radial velocity components after the TRT, whereas the velocity and acceleration components both exist in the cross terms. Assume that the searching velocity ambiguity number is equal to  $M_{v,l}$ , and then the results in (36a) after performing the KT can be expressed as

$$s_{\text{TRT-KT}}(f_r, t_a) = \sigma_l^2 \exp \left( -j \frac{8\pi}{\lambda} v_{b,l} t_a \right) + \sum_{i=1, i \neq l}^I \sigma_i^2 \exp \left( -j \frac{8\pi}{\lambda} v_{b,i} t_a \right) \times \exp \left[ -j \frac{4\pi f_r}{c} (M_{v,i} - M_{v,l}) t_a \right] + \sum_{l=1}^{I-1} \sum_{q=l+1}^I s_{\text{TRT-KT-}l,q\text{-cross}}(f_r, t_a) \quad (37)$$

where  $s_{\text{TRT-KT-}l,q\text{-cross}}(f_r, t_a)$  are the cross terms, which can be found in Appendix III. From (37), it is observed that the coupling relationship between the range frequency and azimuth time of the  $l$ th target is eliminated after KT and phase compensation in (25) with  $M_{v,l}$ , whereas residual coupling still exists for the rest of targets due to the difference of ambiguity numbers. In addition, the residual the first- and second-order RM and DFM still appear in the cross terms of (37), indicating that the cross terms may not be finely focused as the autoterms.

Assume that the radial velocity is estimated precisely, and then take the velocity compensation of the  $l$ th target as an example. The corresponding result is noted as follows:

$$s(f_r, t_m) = \sigma_l \exp \left[ -j \frac{4\pi(f_r + f_c)}{c} \left( R_l + \frac{1}{2} \alpha_l t_m^2 \right) \right] + \sum_{i=1, i \neq l}^I \sigma_i \exp \left\{ -j \frac{4\pi(f_r + f_c)}{c} \left[ R_i + (v_i - v_l) t_m + \frac{1}{2} \alpha_i t_m^2 \right] \right\}. \quad (38)$$

The results after performing FRT can be expressed as

$$s_{\text{FRT}}(f_r, t_m) = \sigma_l^2 \exp \left[ -j \frac{8\pi}{\lambda} \left( R_l + \frac{1}{2} \alpha_l t_m^2 \right) \right] + \sum_{i=1, i \neq l}^I \sigma_i^2 \exp \left[ -j \frac{8\pi}{\lambda} \left( R_i + (v_i - v_l) t_m + \frac{1}{2} \alpha_i t_m^2 \right) \right] + \sum_{l=1}^{I-1} \sum_{q=l+1}^I s_{\text{FRT-}l,q\text{-cross}}(f_r, t_m) \quad (39)$$

where  $s_{\text{FRT-}l,q\text{-cross}}(f_r, t_m)$  are the cross terms, which can be found in Appendix III. Then, after performing the IFT along the

range frequency, one can obtain

$$\begin{aligned}
 s_{\text{FRT}}(t_r, t_m) &= \sigma_l^2 \sin c(Bt_r) \exp \left[ -j \frac{8\pi}{\lambda} \left( R_l + \frac{1}{2} \alpha_l t_m^2 \right) \right] \\
 &+ \sum_{i=1, i \neq l}^I \sigma_i^2 \sin c(Bt_r) \\
 &\times \exp \left[ -j \frac{8\pi}{\lambda} \left( R_i + (v_i - v_l) t_m + \frac{1}{2} \alpha_i t_m^2 \right) \right] \\
 &+ \sum_{l=1}^{I-1} \sum_{q=l+1}^I s_{\text{FRT-}l, q\text{-cross}}(t_r, t_m) \quad (40)
 \end{aligned}$$

where  $s_{\text{FRT-}l, q\text{-cross}}(t_r, t_m)$  are the cross terms (see Appendix III). It can be observed that the autoterms of the  $l$ th target contains only the second-order phases, which will be focused after performing the phase compensation and NUFFT. On the contrary, the cross terms cannot well be accumulated due to the existence of RM and DFM simultaneously. Thus, when the proposed target integration detection and estimation algorithm is applied, the smeared cross terms cannot be accumulated as the autoterms.

## VI. EXPERIMENTAL RESULTS AND ANALYSIS

In this section, both the simulated and real data processing results are provided to demonstrate the effectiveness of the proposed method, where some compared methods are considered.

### A. Simulation Processing Results

The simulation results for a single moving target and multiple targets are given and analyzed. Comparisons with other well-known coherent integration algorithms, including the RFT method, KTMF method, and GRFT method are also given. Then, some performance analyses, such as the output SNR, detection performance, and motion parameter estimation are provided for comparison. It should be noted that the radar system parameters keep the same as listed in Table I.

1) *Simulation Results for a Single Moving Target:* In this section, the coherent integration performance of the proposed method for a high-speed single-moving target is carried out in the presence of complex Gaussian white noise. The motion parameters of this maneuvering target is set as  $[R_0, v, \alpha] = [100 \text{ km}, 200 \text{ m/s}, 120 \text{ m/s}^2]$ , and the target's SNRs are 0.2 and 15 dB before and after the pulse compression, respectively. Based on the radar and target motion parameters, the velocity ambiguity number induced by target radial velocity and the maximum Doppler aliasing number caused by acceleration are calculated as 4 and 2 according to (7).

The echo data after PC is shown in Fig. 8(a), from which one can notice that the severe range walk and range curvature are present. Fig. 8(b) shows the azimuth accumulation results after directly performing the azimuth FFT on the range-compressed target signal in Fig. 8(a). Obviously, this target is significantly smeared along the range and azimuth due to the RM and DFM. In addition, the target spectrum spreads multiple PRF due to the Doppler ambiguity. The range profile after TRT is shown

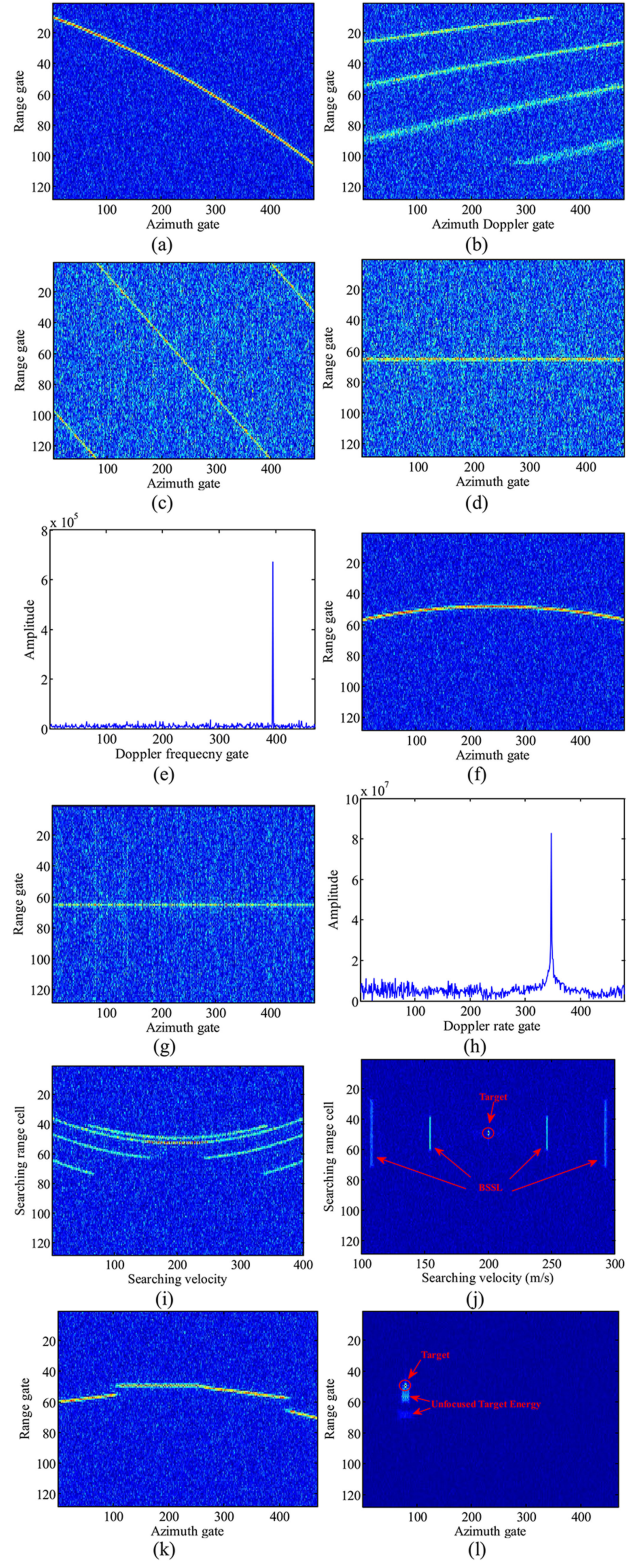


Fig. 8. Simulation results for a moving target. (a) Range profiles after PC. (b) Direct azimuth FFT accumulation. (c) Range profiles after TRT operation. (d) Range profiles after KT with the optimal velocity ambiguity number. (e) Accumulation results via FFT at the range gate  $t_r = 0$ . (f) Range profiles after phase compensation by velocity estimation. (g) Range profiles after FRT. (h) Accumulation results via NUFFT at the range gate  $t_r = 0$  with the optimal Doppler aliasing number. (i) Focused result by the RFT method. (j) Focused result by the GRFT method. (k) Range profiles after KT with optimal acceleration searching results by the KTMF method. (l) Focused result by the KTMF method.

TABLE III  
COMPUTATIONAL TIME EVALUATION

Methods	GRFT	KT matched filtering	RFT	Proposed
Time (s)	729.5s	6.7s	7.1s	1.3s

in Fig. 8(c), which indicates that only linear range walk is reserved and doubled. In spite of aggravated linear range walk, it can be resolved by applying the modified KT given in (21) and (22). Fig. 8(d) shows the results after KT with  $\hat{M}_v = 8$ , as we can see that the energy of this target located at  $t_r = 0$ , as forecasted by (23). The accumulation result is shown in Fig. 8(e) by taking the FFT along the slow time at  $t_r = 0$ . The unambiguous velocity is estimated as  $-7.75$  m/s, and the velocity is calculated as  $199.98$  m/s by (24), which is close to its true value. Fig. 8(f) shows the range profile after compensating the radial velocity influence according to (25). It is observed that the phase terms caused by radial velocity are eliminated and only range curve is reserved. After the FRT operation, the range curve is compensated although the spectrum aliasing occurs, as shown in Fig. 8(g). After performing the phase compensation by (31) and NUFFT, Fig. 8(h) shows the finally imaged result, and a sharp peak is present, from which the acceleration is estimated as  $119.98$  m/s<sup>2</sup> with the maximum Doppler aliasing number being 4. The results of RFT and GRFT are provided in Fig. 8(i) and (j), respectively. Obviously, the RFT is invalid because the acceleration cannot be handled. In addition, the BSSL occurs by using the GRFT method due to the Doppler ambiguity. The results by the KTMF method are shown in Fig. 8(k)–(l). As analyzed in Section III, the segmented characteristic is exhibited after performing the KT; thus only part of the target energy is focused, which may affect the subsequent target detection performance, as shown in Fig. 8(l).

Furthermore, the computation times of these methods are listed in Table III. The simulation environment parameters in this simulation are given as follows: the CPU is Intel Core i5-7300HQ with clocked frequency at 2.5 GHz, and the size of random access memory is 8 GB. As analyzed in Section V-A, the GRFT method has the highest computation amount due to the multidimensional search process. The RFT and KTMF methods require 1-D search, resulting in the low efficiency. The proposed method is computationally efficient since the grid searching process is avoided.

2) *Simulation Results for Multiple Targets:* In this part, the simulation results for multiple targets are given and analyzed in the real sea clutter background, instead of the simulated Gaussian white noise. The motion parameters of a maneuvering target are listed in Table IV.

The processing results by the proposed method for multiple targets with energy crossover are shown in Fig. 9. Range profiles for two moving targets after PC are given in Fig. 9(a), from which one can see that the real-measured sea clutter exists in the radar echoes. The range profiles after the TRT operation are shown in Fig. 9(b), and it can be observed that autoterms only involve the linear range walk. Besides, the cross terms appear in this case, which contain range walk and range curve simultaneously, as analyzed in Section V-B. The target detection results of Target

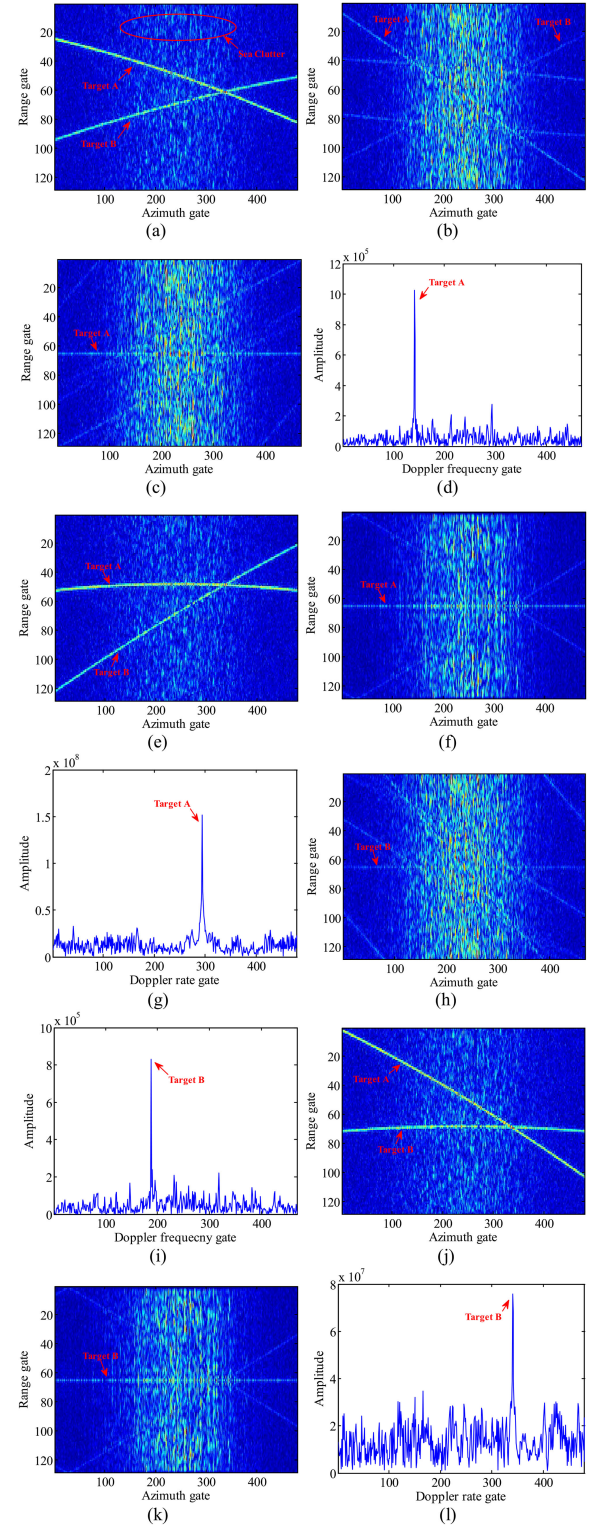


Fig. 9. Simulation results for multiple moving targets. (a) Range profiles after PC. (b) Range profiles after TRT operation. (c) Range profiles after KT with the optimal velocity ambiguity number of Target A. (d) Accumulation results via FFT at the range gate  $t_r = 0$ . (e) Range profiles after phase compensation by velocity estimation of Target A. (f) Range profiles after FRT. (g) Accumulation results via NUFFT at the range gate  $t_r = 0$  with the optimal Doppler aliasing number of Target A. (h) Range profiles after TRT operation and KT with the optimal velocity ambiguity number of Target B. (i) Accumulation results via FFT at the range gate  $t_r = 0$  of Target B. (j) Range profiles after phase compensation by velocity estimation of Target B. (k) Range profiles after FRT. (l) Accumulation results via NUFFT at the range gate  $t_r = 0$  with the optimal Doppler aliasing number of Target B.

TABLE IV  
TARGET MOTION PARAMETERS

Motion Parameters	Target A	Target B
Initial slant range	20km	20.05km
Radial velocity	120m/s	-90m/s
Radial acceleration	60m/s <sup>2</sup>	45m/s <sup>2</sup>
Statistical SCNR (after PC)	13dB	10dB

TABLE V  
PARAMETERS ESTIMATION RESULTS

Motion Parameters	Target A	Target B
Real radial velocity	120 m/s	-90 m/s
Estimated radial velocity	119.99 m/s	-90.02 m/s
Real radial acceleration	60 m/s <sup>2</sup>	45 m/s <sup>2</sup>
Estimated radial acceleration	59.98 m/s <sup>2</sup>	44.96 m/s <sup>2</sup>

A are shown in Fig. 9(c)–(g). When the searching velocity ambiguity number satisfies  $\hat{M}_{v,1} = 5$ , the range walk correction can be well accomplished by the modified KT, as shown in Fig. 9(c). Obviously, this moving target can be well focused after performing the azimuth FFT, as depicted in Fig. 9(d). According to the peak position in Fig. 9(d), the velocity estimation of Target A is calculated as 119.99 m/s based on (24). The phase compensation results by (25) using velocity estimation are exhibited in Fig. 9(e) and the influences of velocity terms are removed. Fig. 9(f) provides the range profile after FRT, and it can be seen that range walk is completely eliminated. Then NUFFT results at the range gate of  $t_r = 0$  are given in Fig. 9(g), from which it is observed that Target A is accumulated as a distinct peak point, with the position providing the estimation of target acceleration, i.e., 59.98 m/s<sup>2</sup> and  $\hat{M}_{\alpha,1} = 2$ . Similar to Target A, the target detection results of Target B are shown in Fig. 9(h)–(l). The searching velocity and Doppler aliasing number of Target B are estimated as  $\hat{M}_{v,2} = -4$  and  $\hat{M}_{\alpha,2} = 2$ , respectively. Then, the velocity and acceleration can be estimated as -90.02 m/s and 44.96 m/s<sup>2</sup>, respectively, as listed in Table V.

3) *Performance Analysis*: In this part, the output SNR, detection performance and parameters estimation precision for the RFT method, KTMF method, GRFT method and proposed method are compared under different SNRs. The radar parameters are the same as those listed in Table I. The motion parameters of a maneuvering target is set as  $[R_0, v, \alpha] = [50 \text{ km}, 300 \text{ m/s}, 120 \text{ m/s}^2]$ . The scope of the target's SNR (after PC) varies from -10 to 10 dB with a step of 2 dB, and the number of Monte Carlo simulation is 100, where the false alarm ratio is set as  $P_{fa} = 10^{-6}$ . In this simulation, the amplitude detection threshold can be obtained by performing the Monte Carlo experiments according to the given false alarm and simulation environment. Suppose that the size of the simulated scene is  $M \times N$ , count and rank the amplitude for noise scene, using  $\text{Amp}_{\text{noise}}$  to express the noise amplitude in a descending order. Then, the detection threshold can be determined by

$$\hat{V}_T = \text{Amp}_{\text{noise}} [\text{round}(P_{fa} \cdot M \cdot N)] \quad (41)$$

where  $\hat{V}_T$  denotes the measured detection method, and  $\text{round}(\cdot)$  means the round operation.

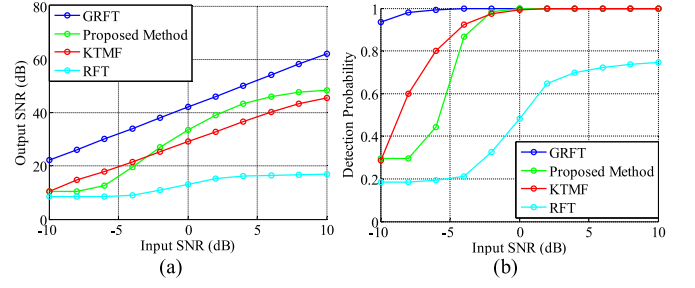


Fig. 10. Output SNR and detection probability curves against SNR. (a) Output SNR varies input SNR. (b) Detection probability varies input SNR.

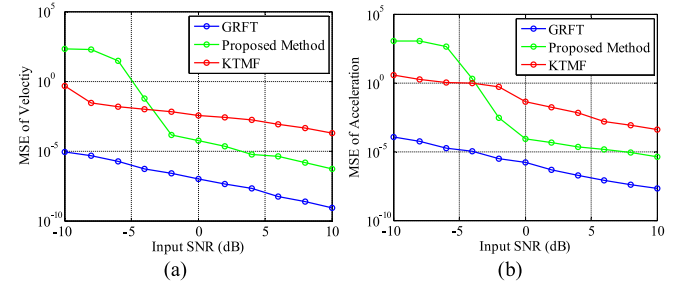


Fig. 11. Velocity and acceleration estimation errors against SNR. (a) MSE of velocity estimation varies with the input SNR. (b) MSE of acceleration estimation varies with the input SNR.

In addition, when the amplitude distribution of the detection background is known as *a priori*, the amplitude detection threshold can be theoretically obtained based on a constant false alarm. For example, assume that Gaussian white noise background is considered, and then the amplitude detection threshold  $V_T$  can be theoretically set as follows [43]:

$$V_T = \sqrt{2\sigma_n^2 \ln\left(\frac{1}{P_{fa}}\right)} \quad (42)$$

where  $\sigma_n^2$  is the noise variance.

As depicted in Fig. 10, the GRFT method provides the optimal detection performance since it is designed based on the maximum likelihood estimator. The proposed method is superior to the KTMF method under the higher SNR environment (upon -2 dB), due to fact that all the energy of target is used in the proposed method while only part of energy is utilized in the KT matched filtering method. With the decrease of SNR, the energy loss caused by nonlinear operation becomes larger, resulting in the detection performance decline. The RFT method shows the poor detection performance because of the non-stationary phase influence.

Fig. 11 shows the MSE of velocity and acceleration estimation varying with the input SNR, from which it can be observed that the trend is similar to the curve in Fig. 10. It is because the accuracy of parameter estimation is deeply relied on the input SNR.

### B. Real Data Processing Results

In this section, experiments on the spaceborne SAR real data are shown to further verify the validity of the proposed

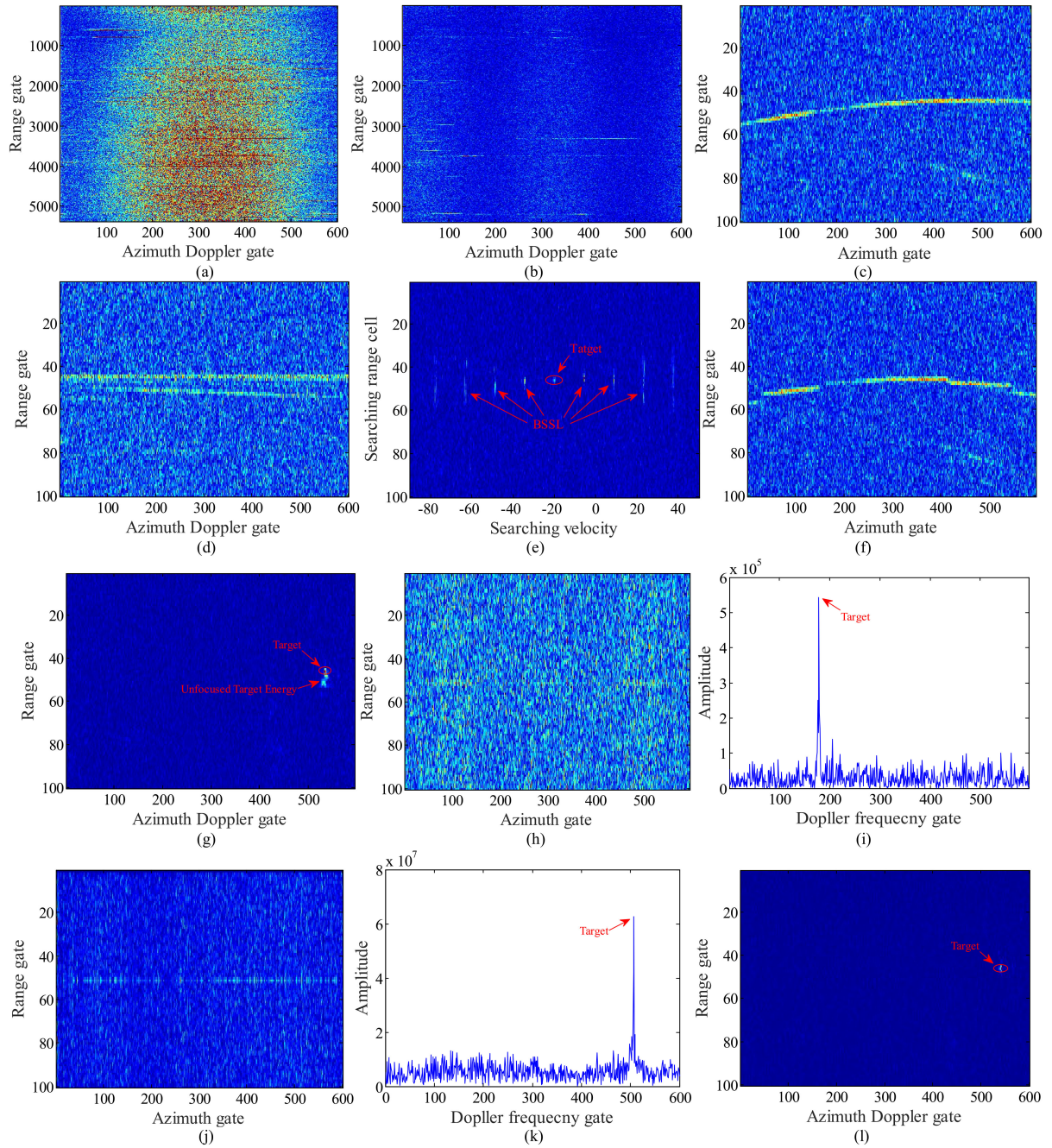


Fig. 12. Real data processing results in a real SBR system. (a) Doppler spectrum before clutter rejection. (b) Doppler spectrum after clutter rejection. (c) Range profile for target from 2901–3000 range gate. (d) Doppler spectrum with selected target. (e) Focused result by the GRFT method. (f) Range profiles after KT with optimal acceleration searching results by the KTMF method. (g) Focused result by the KTMF method. (h) Range profiles after TRT and KT with the velocity ambiguity number  $-3$ . (i) Accumulation results via FFT at the range gate  $t_r = 0$ . (j) Range profiles after phase compensation by (25) and the FRT. (k) Accumulation results via NUFFT at the range gate  $t_r = 0$  with the Doppler aliasing number 2. (l) Final focusing results with the proposed method.

method. The data are recorded by C-band Gaofen-3 satellite system of China with dual receiving channel, which works in a broadside mode. The wavelength of Gaofen-3 experiment is 0.0054 m with PRF 533.3 Hz, and the range bandwidth and range sample frequency are 60 and 66.66 MHz, respectively. As shown in Fig. 12(a), clutter spectrum in spaceborne radar (SBR) echoes is seriously extended due to the high speed of a spaceborne platform. After clutter suppression by using

post-Doppler space-time adaptive processing (STAP) method in [44] and [45], Fig. 12(b) shows the clutter residue in the range-Doppler domain. It can be observed that the most of the clutter is effectively suppressed, and several moving targets become visible. After selecting a moving target from 2900 to 3000 range cell in Fig. 12(b), the motion envelope trajectory of this target in the 2-D time domain is shown in Fig. 12(c). One can see that both RM and range curve exist for this target. The Doppler

spectrum of this target is shown in Fig. 12(d), from which it can be seen that several Doppler aliasing occurs, and target cannot be detected effectively. Fig. 12(e) shows the target detection results with GRFT methods by searching the velocity and acceleration, from which one can see that target is detected while serious BSSL occurs. The detection results with the KTMF method are shown in Fig. 12(f) and (g). As shown in Fig. 12(f), the piecewise range walks appear after performing the KT, as analyzed in (16). Only the energy of unambiguous part is accumulated in the KTMF method, as depicted in Fig. 12(g). Fig. 12(h)–(l) shows the results by the proposed method. The range profile after TRT and KT with ambiguity number  $-3$  is shown in Fig. 12(h), and the target trajectory is hardly observed due to the residual clutter and energy loss caused by the nonlinear operation. Nonetheless, the moving target can be detected after coherent accumulation by performing the azimuth FFT, and the velocity is estimated as  $-20.11$  m/s by (24). Fig. 12(j) shows the range profile after compensating the influence of velocity performing the FRT, from which it is seen that the range profile locate at  $t_r = 0$ , as forecasted in (25). After compensating the phase term with (26) and performing the NUFFT, the accumulation results are shown in Fig. 12(k), and the velocity is calculated as  $28.71$  m/s by (34). A well-focused target can be found in the final focusing result, which is depicted in Fig. 12(l). As a result, the proposed method can be also applicable to achieve the target detection and parameter estimation for a real SBR system with the target Doppler aliasing.

## VII. CONCLUSION

In this article, the problem of coherent accumulation for the Doppler aliasing targets is analyzed. To address the velocity ambiguity and Doppler spectrum aliasing of a maneuvering target, a novel searching-free algorithm is proposed in this article. By utilizing the symmetry of time, TRT is used to separate the velocity and acceleration, and thus the proposed method can handle the Doppler ambiguity and Doppler aliasing target individually. Then, velocity estimation can be obtained by using the KT. After that, the acceleration estimation can be achieved by the FRT and NUFFT. Therefore, the proposed method is computationally efficient and can achieve the effective coherent accumulation for a maneuvering target. However, the nonlinear operation is required in our proposed, resulting in the performance loss under the low SNR. How to effectively and efficiently deal with a moving target with velocity ambiguity and Doppler aliasing under the low SCNR without the nonlinear operation is under our future research. Furthermore, in the next investigation, we will discuss the application of the proposed algorithm to the detection and imaging for high-speed noncooperative target scenes, i.e., SAR-ground moving target indication mode and inverse SAR imaging field.

## APPENDIX I

Without loss of generality, the relation between a signal with Doppler aliasing times  $M_\alpha$  and an unambiguous signal is deduced in this appendix.

For a signal at the unambiguous time of  $[-T_a/(2M_s), T_a/(2M_s)]$ , it can be expressed as

$$S_0(f_r, t_m) = \sigma \text{rect}\left(\frac{f_r}{B}\right) \text{rect}\left(\frac{t_{m,0}}{T_a/M_s}\right) \times \exp\left[-j\frac{4\pi(f_r + f_c)}{c}\left(R_0 + \frac{1}{2}\alpha t_{m,0}^2\right)\right] \quad (43)$$

where  $t_{m,0} \in [-T_a/(2M_s), T_a/(2M_s)]$  denotes the unambiguous time variable in this case.

For the signal at the Doppler aliasing times of  $M_\alpha$  time, one has

$$S_{M_\alpha}(f_r, t_m) = \sigma \text{rect}\left(\frac{f_r}{B}\right) \text{rect}\left(\frac{t_{m,M_\alpha}}{T_a/M_s}\right) \times \exp\left[-j\frac{4\pi(f_r + f_c)}{c}\left(R_0 + \frac{1}{2}\alpha t_{m,M_\alpha}^2\right)\right] \quad (44)$$

where the time slicing  $t_{m,M_\alpha} = t_{m,0} + M_\alpha \frac{T_a}{M_s}$ .

Substituting  $t_{m,M_\alpha}$  into (44), one can obtain

$$S_{M_\alpha}(f_r, t_m) = \sigma \text{rect}\left(\frac{f_r}{B}\right) \text{rect}\left(\frac{t_{m,0} + M_\alpha \frac{T_a}{M_s}}{T_a/M_s}\right) \times \exp\left[-j\frac{4\pi(f_r + f_c)}{c}\left(R_0 + \frac{1}{2}\alpha t_{m,0}^2\right)\right] \times \exp\left[-j\frac{2\pi f_r}{f_c} M_\alpha \text{PRF} t_{m,0}\right] \times \exp\left[-j\frac{\pi(f_r + f_c)}{f_c} M_\alpha^2 \text{PRF} \frac{T_a}{M_s}\right]. \quad (45)$$

According to (45), a Doppler aliasing signal in (12) can be written as a form of summation, as depicted in (15).

## APPENDIX II

The NUDFT of a nonuniform signal  $z_l$  is expressed as

$$\hat{z}_k = \sum_{l=1}^M z_l \exp(-j2\pi x_l k/N), \quad k = -N/2, \dots, N/2 + 1 \quad (46)$$

where  $z_l$  is the nonuniformly sampled data in the time domain,  $x_l$  is the corresponding nonuniform sampling position, and  $\hat{z}_k$  is the uniform output signal in the frequency domain. Instead of interpolating the nonuniform sampled data  $z_l$ , the exponential terms are interpolated to implement the NUFFT. The exponential signal can be expanded as follows [40]:

$$\exp(-jx\xi) = \frac{(2\pi)^{-1/2}}{\phi(\xi)} \sum_{m \in \mathbb{Z}} \hat{\phi}(x - m) \exp(-jm\xi) \quad (47)$$

where  $x = cx_l$  and  $\xi = 2\pi k/cN$  with an oversampling factor  $c$ , which satisfies  $|\xi| \leq \pi/c$ .  $\hat{\phi}(x)$  and  $\phi(\xi)$  are a Fourier transform pair of a window function. Typically, a Kaiser-Bessel window

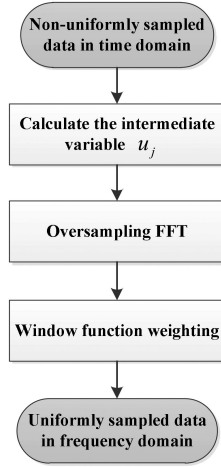


Fig. 13. Schematic diagram of NUFFFT implementation.

function [46] is used in this article, which is defined as

$$\hat{\phi}(x) = \sqrt{\frac{2}{\pi}} \frac{\sinh(\alpha\sqrt{K^2 - x^2})}{(\sqrt{K^2 - x^2})}, \quad -K \leq x \leq K \quad (48)$$

$$\phi(\xi) = \begin{cases} I_0(K\sqrt{\alpha^2 - \xi^2}), & |\xi| \leq \alpha \\ 0, & |\xi| > \alpha \end{cases} \quad (49)$$

where  $K$  is interpolating kernel length and  $\alpha$  is the width of window function and set as  $\alpha = \pi(2 - 1/c) - 0.01$ .

Substituting (48) into (47), we can obtain a uniform output signal in the frequency domain, i.e.,

$$\hat{z}_k = \frac{1}{\phi_k} \sum_{i=-cN/2}^{cN/2-1} u_i \exp(-j2\pi ki/cN) \quad (50)$$

where  $u_i = \sum_{l=1}^M \sum_{m \in Z} z_l \hat{\phi}_{l,i+cmN-\mu_l}$  is the intermediate variable,  $\phi_k = \phi(2\pi k/cN)$ , and  $\hat{\phi}_{lm} = \frac{1}{2\pi} \hat{\phi}(cx_l - (\mu_l + m))$ . The implementation process of NUFFFT is shown in Fig. 13.

### APPENDIX III

In this appendix, the cross terms in (36a), (37), (39), and (40) are provided. Consider two arbitrary moving targets, i.e.,  $l \in [1, I-1]$  and  $q \in [l+1, I]$ . After performing the TRT, the cross terms in (36a) are exhibited as follows:

$$s_{\text{TRT-}l,q\text{-cross}}(f_r, t_m) = \sigma_l \sigma_q \exp \left[ -j \frac{4\pi(f_r + f_c)}{c} \Delta R_1(t_m) \right] + \sigma_l \sigma_q \exp \left[ -j \frac{4\pi(f_r + f_c)}{c} \Delta R_2(t_m) \right] \quad (51)$$

with

$$\Delta R_1(t_m) = (R_l - R_q) + (v_l + v_q) t_m + \frac{1}{2} (\alpha_l - \alpha_q) t_m^2 \quad (52)$$

$$\Delta R_2(t_m) = (R_q - R_l) + (v_q + v_l) t_m + \frac{1}{2} (\alpha_q - \alpha_l) t_m^2. \quad (53)$$

After performing the KT on (51), one has

$$s_{\text{TRT-KT-}l,q\text{-cross}}(f_r, t_a) = \sigma_l \sigma_q \exp \left[ -j \frac{4\pi(f_r + f_c)}{c} (R_l - R_q) \right] \times \exp \left[ -j \frac{4\pi}{\lambda} (v_{b,l} + v_{b,q}) t_a \right] \times \exp \left[ -j \frac{4\pi f_r}{c} M_{v,q} t_a \right] \times \exp \left\{ -j \frac{2\pi f_c^2}{c(f_r + f_c)} (\alpha_l - \alpha_q) t_a^2 \right\} + \sigma_l \sigma_q \exp \left[ -j \frac{4\pi(f_r + f_c)}{c} (R_q - R_l) \right] \times \exp \left[ -j \frac{4\pi}{\lambda} (v_{b,l} + v_{b,q}) t_a \right] \times \exp \left[ -j \frac{4\pi f_r}{c} M_{v,q} t_a \right] \times \exp \left\{ -j \frac{2\pi f_c^2}{c(f_r + f_c)} (\alpha_q - \alpha_l) t_a^2 \right\} \quad (54)$$

where  $v_{b,l}$  and  $v_{b,q}$  are the unambiguous velocity of the  $l$ th and  $q$ th targets, and  $M_{v,q}$  is the velocity ambiguity number induced by the  $q$ th target radial velocity.

The cross terms in (39) can be expressed as follows:

$$s_{\text{FRT-}l,q\text{-cross}}(f_r, t_m) = \sigma_l \sigma_q \exp \left[ -j \frac{4\pi f_r}{c} \Delta R_3(t_m) \right] \times \exp \left[ -j \frac{4\pi}{\lambda} \Delta R_4(t_m) \right] + \sigma_l \sigma_q \exp \left[ j \frac{4\pi f_r}{c} \Delta R_3(t_m) \right] \times \exp \left[ -j \frac{4\pi}{\lambda} \Delta R_4(t_m) \right] \quad (55)$$

with

$$\Delta R_3(t_m) = (R_l - R_q) + (v_l - v_q) t_m + \frac{1}{2} (\alpha_l - \alpha_q) t_m^2 \quad (56)$$

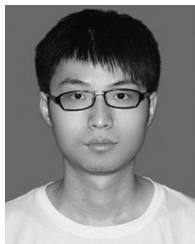
$$\Delta R_4(t_m) = (R_l + R_q) + (v_q - v_l) t_m + \frac{1}{2} (\alpha_l + \alpha_q) t_m^2. \quad (57)$$

After performing the IFFT on (55) along the range frequency variable, one has

$$s_{\text{FRT-}l,q\text{-cross}}(t_r, t_m) = \sigma_l \sigma_q \sin c \left[ B \left( t_r - \frac{2\Delta R_3(t_m)}{c} \right) \right] \times \exp \left[ -j \frac{4\pi}{\lambda} \Delta R_4(t_m) \right] + \sigma_l \sigma_q \sin c \left[ B \left( t_r + \frac{2\Delta R_3(t_m)}{c} \right) \right] \times \exp \left[ -j \frac{4\pi}{\lambda} \Delta R_4(t_m) \right]. \quad (58)$$

## REFERENCES

- [1] X. L. Chen, Y. Huang, N. B. Liu, J. Guan, and Y. He, "Radon-fractional ambiguity function-based detection method of low-observable maneuvering target," *IEEE Trans. Aerosp. Electron. Syst.*, vol. 51, no. 2, pp. 815–833, Apr. 2015.
- [2] X. L. Li, G. Cui, L. Kong, and W. Yi, "Fast non-searching method for maneuvering target detection and motion parameters estimation," *IEEE Trans. Signal Process.*, vol. 64, no. 9, pp. 2232–2244, May 2016.
- [3] J. Su, M. Xing, G. Wang, and Z. Bao, "High-speed multi-target detection with narrowband radar," *IET Radar, Sonar Navig.*, vol. 4, no. 4, pp. 595–603, Aug. 2010.
- [4] G. Li, X.-G. Xia, J. Xu, and Y. N. Peng, "A velocity estimation algorithm of moving targets using single antenna SAR," *IEEE Trans. Aerosp. Electron. Syst.*, vol. 45, no. 3, pp. 1052–1062, Jul. 2009.
- [5] J. Tian, W. Cui, and S. Wu, "A novel method for parameter estimation of space moving targets," *IEEE Geosci. Remote Sens. Lett.*, vol. 11, no. 2, pp. 389–393, Feb. 2014.
- [6] R. P. Perry, R. C. DiPietro, and R. L. Fante, "SAR imaging of moving targets," *IEEE Trans. Aerosp. Electron. Syst.*, vol. 35, no. 1, pp. 188–200, Jan. 1999.
- [7] S. S. Zhang, T. Zeng, T. Long, and H. P. Yuan, "Dim target detection based on keystone transform," in *Proc. IEEE Int. Radar Conf.*, May 2005, pp. 889–894.
- [8] J. Xu, J. Yu, Y. N. Peng, and X.-G. Xia, "Radon-Fourier transform for radar target detection, I: Generalized Doppler filter bank," *IEEE Trans. Aerosp. Electron. Syst.*, vol. 47, no. 2, pp. 1186–1202, Apr. 2011.
- [9] J. Xu, J. Yu, Y. N. Peng, and X.-G. Xia, "Radon-Fourier transform for radar target detection (II): Blind speed sidelobe suppression," *Aerosp. Electron. Syst.*, vol. 47, no. 4, pp. 2473–2489, Oct. 2011.
- [10] X. Rao, H. H. Tao, J. Su, X. L. Guo, and J. Z. Zhang, "Axis rotation MTD algorithm for weak target detection," *Digit. Signal Process.*, vol. 26, pp. 81–86, Mar. 2014.
- [11] J. B. Zheng, T. Su, W. T. Zhu, X. H. He, and Q. H. Liu, "Radar high-speed target detection based on the scaled inverse Fourier transform," *IEEE J. Sel. Topics Appl. Earth Observ. Remote Sens.*, vol. 8, no. 3, pp. 1108–1119, Mar. 2015.
- [12] J. B. Zheng, T. Su, H. W. Liu, G. S. Liao, Z. Liu, and Q. H. Liu, "Radar high-speed target detection based on the frequency-domain Deramp-Keystone transform," *IEEE J. Sel. Topics Appl. Earth Observ. Remote Sens.*, vol. 9, no. 1, pp. 285–294, Jan. 2016.
- [13] J. Carretero-Moya, J. Gismero-Menoyo, A. Asensio-Lopez, and A. Blanco-del-Campo, "Application of the Radon transform to detect small targets in sea clutter," *IET Radar, Sonar Navig.*, vol. 3, no. 2, pp. 155–166, Apr. 2009.
- [14] Y. K. Kong, B. L. Cho, and Y. S. Kim, "Ambiguity-free Doppler centroid estimation technique for airborne SAR using the Radon transform," *IEEE Trans. Geosci. Remote Sens.*, vol. 43, no. 4, pp. 715–721, Apr. 2005.
- [15] B. D. Carlson, E. D. Evans, and S. L. Wilson, "Search radar detection and track with the Hough transform, Part I: System concept," *IEEE Trans. Aerosp. Electron. Syst.*, vol. 30, no. 1, pp. 102–108, Jan. 1994.
- [16] B. D. Carlson, E. D. Evans, and S. L. Wilson, "Search radar detection and track with the Hough transform. II. Detection statistics," *IEEE Trans. Aerosp. Electron. Syst.*, vol. 30, no. 1, pp. 109–115, Jan. 1994.
- [17] B. D. Carlson, E. D. Evans, and S. L. Wilson, "Search radar detection and track with the Hough transform. III. Detection performance with binary integration," *IEEE Trans. Aerosp. Electron. Syst.*, vol. 30, no. 1, pp. 116–125, Jan. 1994.
- [18] J. Xu, X.-G. Xia, S.-B. Peng, J. Yu, Y.-N. Peng, and L.-C. Qian, "Radar maneuvering target motion estimation based on generalized Radon-Fourier transform," *IEEE Trans. Signal Process.*, vol. 60, no. 12, pp. 6190–6201, Dec. 2012.
- [19] X. L. Chen, J. Guan, N. B. Liu, and Y. He, "Maneuvering target detection via Radon-fractional Fourier transform-based long-time coherent integration," *IEEE Trans. Signal Process.*, vol. 62, no. 4, pp. 939–953, Feb. 2014.
- [20] X. L. Li, G. L. Cui, W. Yi, and L. J. Kong, "Coherent integration for maneuvering target detection based on Radon-Lv's distribution," *IEEE Signal Process. Lett.*, vol. 22, no. 9, pp. 1467–1471, Sep. 2015.
- [21] J. Tian, W. Cui, X.-G. Xia, and S. L. Wu, "Parameter estimation of ground moving targets based on SKT-DLVT processing," *IEEE Trans. Comput. Imag.*, vol. 2, no. 1, pp. 13–26, Mar. 2016.
- [22] X. L. Chen, J. Guan, N. B. Liu, W. Zhou, and Y. He, "Detection of a low observable sea-surface target with micromotion via the Radon-linear canonical transform," *IEEE Geosci. Remote Sens. Lett.*, vol. 11, no. 7, pp. 1225–1229, Jul. 2014.
- [23] P. H. Huang, G. S. Liao, Z. Yang, X.-G. Xia, J.-T. Ma, and X. Zhang, "A fast SAR imaging method for ground moving target using a second-order WVD transform," *IEEE Trans. Geosci. Remote Sens.*, vol. 54, no. 4, pp. 1940–1956, Apr. 2016.
- [24] D. Li, X. G. Gui, H. Q. Liu, J. Su, and H. Xiong, "An ISAR imaging algorithm for maneuvering targets with low SNR based on parameter estimation of multicomponent quadratic FM signals and nonuniform FFT," *IEEE J. Sel. Topics Appl. Earth Observ. Remote Sens.*, vol. 9, no. 12, pp. 5688–5702, Dec. 2016.
- [25] X.-G. Xia, "On band limited signals with fractional Fourier transform," *IEEE Signal Process. Lett.*, vol. 3, no. 3, pp. 72–74, Mar. 1996.
- [26] X.-G. Xia, "A quantitative analysis of SNR in the short-time Fourier transform domain for multicomponent signals," *IEEE Trans. Signal Process.*, vol. 46, no. 1, pp. 200–203, Jan. 1998.
- [27] S. Q. Zhu, G. S. Liao, Y. Qu, Z. G. Zhou, and X. Y. Liu, "Ground moving targets imaging algorithm for synthetic aperture radar," *IEEE Trans. Geosci. Remote Sens.*, vol. 49, no. 1, pp. 462–477, Jan. 2011.
- [28] Y. L. Neo, F. Wong, and I. G. Cumming, "A two-dimensional spectrum for bistatic SAR processing using series reversion," *IEEE Geosci. Remote Sens. Lett.*, vol. 4, no. 1, pp. 93–96, Jan. 2007.
- [29] Z. Sun, X. L. Li, W. Yi, G. L. Cui, and L. J. Kong, "Detection of weak maneuvering target based on keystone transform and matched filtering process," *Signal Processing*, vol. 140, pp. 127–138, May 2017.
- [30] P. H. Huang, G. S. Liao, X. Yang, X.-G. Xia, J.-T. Ma, and J. T. Ma, "Long-time coherent integration for weak maneuvering target detection and high-order motion parameter estimation based on keystone transform," *IEEE Trans. Signal Process.*, vol. 64, no. 15, pp. 4013–4026, Aug. 2016.
- [31] F. Zhou, R. Wu, M. Xing, and Z. Bao, "Approach for single channel SAR ground moving target imaging and motion parameter estimation," *IET Radar, Sonar Navig.*, vol. 1, no. 1, pp. 59–66, Feb. 2007.
- [32] J. Tian, W. Cui, and S. Wu, "A novel method for parameter estimation of space moving targets," *IEEE Geosci. Remote Sens. Lett.*, vol. 11, no. 2, pp. 389–393, Feb. 2014.
- [33] D. Kirkland, "Imaging moving targets using the second-order keystone transform," *IET Radar, Sonar Navig.*, vol. 5, no. 8, pp. 902–910, Feb. 2011.
- [34] G. Li, X.-G. Xia, and Y. N. Peng, "Doppler keystone transform for SAR imaging of moving targets," in *Proc. Congr. Image Signal Process.*, 2008, vol. 4, pp. 27–30.
- [35] G. Li, X.-G. Xia, and Y. N. Peng, "Doppler keystone transform: An approach suitable for parallel implementation of SAR moving target imaging," *IEEE Geosci. Remote Sens. Lett.*, vol. 5, no. 4, pp. 573–577, Oct. 2008.
- [36] G. C. Sun, M. D. Xing, X.-G. Xia, Y. R. Wu, and Z. Bao, "Robust ground moving-target imaging using Deramp-Keystone processing," *IEEE Trans. Geosci. Remote Sens.*, vol. 51, no. 2, pp. 966–982, Feb. 2013.
- [37] X. L. Li, L. Kong, G. Cui, and W. Yi, "A fast detection method for maneuvering target in coherent radar," *IEEE Sensors J.*, vol. 15, no. 11, pp. 6722–6729, Nov. 2015.
- [38] S. Q. Zhu, G. S. Liao, D. Yang, and H. H. Tao, "A new method for radar high-speed maneuvering weak target detection and imaging," *IEEE Geosci. Remote Sens. Lett.*, vol. 11, no. 7, pp. 1175–1179, Jul. 2014.
- [39] P. H. Huang, G. S. Liao, Z. W. Yang, Y. X. Shu, and W. T. Du, "Approach for space-based radar manoeuvring target detection and high-order motion parameter estimation," *IET Radar, Sonar Navig.*, vol. 9, no. 6, pp. 732–741, Jun. 2015.
- [40] Q. H. Liu, "An accurate algorithm for nonuniform fast Fourier transforms (NUFFT's)," *IEEE Microw. Guided Wave Lett.*, vol. 8, no. 1, pp. 18–20, Jan. 1998.
- [41] J. Song, Q. H. Liu, P. Torrione, and L. Collins, "Two-dimensional and third-dimensional NUFFT migration method for landmine detection using ground-penetrating radar," *IEEE Trans. Geosci. Remote Sens.*, vol. 44, no. 6, pp. 1462–1469, May 2006.
- [42] D. Zhu, Y. Li, and Z. Zhu, "A Keystone transform without interpolation for SAR ground moving-target imaging," *IEEE Geosci. Remote Sens. Lett.*, vol. 4, no. 1, pp. 18–22, Jan. 2007.
- [43] B. R. Mahafza and A. Z. Elsherbeni, *MATLAB Simulations for Radar Systems Design*. London, U.K.: Chapman & Hall, 2003.
- [44] R. DiPietro, "Extended factored space-time processing for airborne radar systems," in *Proc. 26th Asilomar Conf. Signals, Syst. Comput.*, Oct. 1992, pp. 425–430.
- [45] Z. Y. Li, S. C. Li, Z. T. Liu, H. G. Yang, J. J. Wu, and J. Y. Yang, "Bistatic forward-looking SAR MP-DPCA method for space-time extension clutter suppression," *IEEE Trans. Geosci. Remote Sens.*, in press, pp. 1–15, Mar. 2020.
- [46] D. Krzyśtof, "DFT interpolation algorithm for Kaiser-Bessel and Dolph-Chebyshev windows," *IEEE Trans. Instrum. Meas.*, vol. 60, no. 3, pp. 784–790, Mar. 2011.



**Muyang Zhan** (Graduate Student Member, IEEE) was born in Hubei, China, in 1992. He received the B.S. degree in electronic information engineering from Huanggang Normal University, Hubei, China, in 2015, and the M.S. degree in electronic and information engineering from the Chongqing University, Chongqing, China, in 2018. He is currently working toward the Ph.D. degree with the School of Electronic Information and Electrical Engineering, Shanghai Jiao Tong University, Shanghai, China.

His research interests include inverse SAR imaging, parameter estimation, and spaceborne radar system design.



**Zhijun Zhang** received the B.S. degree in electronic information engineering from Shanghai Polytechnic University, Shanghai, China, and the M.S. degree in software engineering from Dalian University of Technology, Dalian, China.

His research interests include radar signal and information processing.



**Penghui Huang** (Member, IEEE) was born in Jiangxi, China. He received the B.S. and Ph.D. degrees in electrical engineering from Xidian University, Xi'an, China, in 2012 and 2017, respectively.

He joined the School of Electronic Information and Electrical Engineering, Shanghai Jiao Tong University, Shanghai, China, in 2017, where he is currently an Assistant Professor. His research interests include spaceborne radar system design, array signal processing, SAR/inverse SAR imaging, and time–frequency analysis.



**Xingzhao Liu** (Member, IEEE) received the B.S. and M.S. degrees in electrical engineering from Harbin Institute of Technology, Harbin, China, in 1984 and 1992, respectively, and the Ph.D. degree in electrical engineering from the University of Tokushima, Tokushima, Japan, in 1995.

He was an Assistant Professor, an Associate Professor, and a Professor with Harbin Institute of Technology, from 1984 to 1998. Since 1998, he has been a Professor with Shanghai Jiao Tong University, Shanghai, China. His research interests include

high-frequency radar and synthetic aperture radar signal processing.



**Zhicheng Wang** received the B.S. degree in information engineering from Nanjing University of Aeronautics and Astronautics, Nanjing, China, in 2005, and the M.S. degree in signal and information processing from Shanghai Academy of Spaceflight Technology, Shanghai, China. He is currently working toward the Ph.D. degree with the School of Electronic Information and Electrical Engineering, Shanghai Jiao Tong University, Shanghai, China.

His research interests include signal processing for the phased array radar.



**Guisheng Liao** (Senior Member, IEEE) was born in Guiling, China. He received the B.S. degree from Guangxi University, Guangxi, China, and the M.S. and Ph.D. degrees from Xidian University, Xi'an, China, in 1985, 1990, and 1992, respectively.

He is currently a Professor with Xidian University, where he is also the Dean of School of Electronic Engineering. He has been a Senior Visiting Scholar with The Chinese University of Hong Kong, Hong Kong. His research interests include synthetic aperture radar (SAR), space–time adaptive processing, SAR ground

moving target indication, and distributed small satellite SAR system design.

Prof. Liao is a member of the National Outstanding Person and the Cheung Kong Scholars in China.



**Qingyu Hou** received the B.S. and Ph.D. degrees in electronic engineering from Xidian University, Xi'an, China, in 2004 and 2009, respectively.

He is currently a Professor with the 8511 Research Institute of China Aerospace Science and Industry Corporation, Nanjing, China. His research interests include radar signal processing and electronic warfare.